



MIT Open Access Articles

Subwavelength image manipulation through an oblique layered system

The MIT Faculty has made this article openly available. ***Please share*** how this access benefits you. Your story matters.

Citation	Wang, Jin et al. "Subwavelength Image Manipulation Through an Oblique Layered System." <i>Optics Express</i> 19.18 (2011): 16809. ©2011 OSA
As Published	http://dx.doi.org/10.1364/OE.19.016809
Publisher	Optical Society of America
Version	Final published version
Accessed	Thu Jun 15 22:30:59 EDT 2017
Citable Link	http://hdl.handle.net/1721.1/78354
Terms of Use	Article is made available in accordance with the publisher's policy and may be subject to US copyright law. Please refer to the publisher's site for terms of use.
Detailed Terms	

Subwavelength image manipulation through an oblique layered system

Jin Wang,^{1,4,5} Hui Yuan Dong,^{1,2} Kin Hung Fung,^{4,5}
Tie Jun Cui,^{1,3,6} and Nicholas X. Fang^{4,5,*}

¹Department of Physics, Southeast University, Nanjing 211189, China

²School of Science, Nanjing University of Posts and Telecommunications, Nanjing 210003, China

³Current address: State Key Laboratory of Millimeter Waves, Department of Radio Engineering, Southeast University, Nanjing 210096, China

⁴Department of Mechanical Science and Engineering, University of Illinois at Urbana-Champaign, Urbana, IL 61801, USA

⁵Department of Mechanical Engineering, Massachusetts Institute of Technology, Cambridge, MA 02139, USA

⁶tjcui@seu.edu.cn

*nicfang@mit.edu

Abstract: We show in this work an oblique layered system that is capable of manipulating two dimensional subwavelength images. Through properly designed planar layered system, we demonstrate analytically that lateral image shift could be achieved with subwavelength resolution, due to the asymmetry of the dispersion curve of constant frequency. Further, image rotation with arbitrary angle, as well as image magnification could be generated through a concentric geometry of the alternating layered system. In addition, we verify the image mechanism using full wave electromagnetic (EM) simulations. Utilizing the proposed layered system, optical image of an object with subwavelength features can be projected allowing for further optical processing of the image by conventional optics.

© 2011 Optical Society of America

OCIS codes: (110.0180) Microscopy; (160.1190) Anisotropic optical materials.

References and links

1. E. Abbe, "Beitrage zur theorie des mikroskops und der mikroskopischen wahrnehmung," *Arch. Mikrosk. Anat.* **9**, 413–468 (1873).
2. J. B. Pendry, "Negative refraction makes a perfect lens," *Phys. Rev. Lett.* **85**, 3966–3969 (2000).
3. N. Fang, H. Lee, C. Sun, and X. Zhang, "Sub-diffraction-limited optical imaging with a silver superlens," *Science* **308**, 534–537 (2005).
4. T. J. Cui, D. R. Smith, and R. Liu, eds., *Metamaterials—Theory, Design, and Applications* (Springer, 2009).
5. S. A. Ramakrishna, J. B. Pendry, M. C. K. Wiltshire, and W. J. Stewart, "Imaging the near field," *J. Mod. Opt.* **50**, 1419–1430 (2003).
6. S. A. Ramakrishna and J. B. Pendry, "Removal of absorption and increase in resolution in a near-field lens via optical gain," *Phys. Rev. B* **67**, 201101(R) (2003).
7. T. A. Morgado and M. G. Silveirinha, "Transport of an arbitrary near-field component with an array of tilted wires," *New J. Phys.* **11**, 083023 (2009).
8. T. A. Morgado, J. S. Marcos, M. G. Silveirinha, and S. I. Maslovski, "Experimental verification of full reconstruction of the near-field with a metamaterial lens," *Appl. Phys. Lett.* **97**, 144102 (2010).
9. A. Rahman, P. A. Belov, Y. Hao, and C. Parini, "Periscope-like endoscope for transmission of a near field in the infrared range," *Opt. Lett.* **35**, 142–144 (2010).
10. P. A. Belov, C. R. Simovski, and P. Ikonen, "Canalization of subwavelength images by electromagnetic crystals," *Phys. Rev. B* **71**, 193105 (2005).

11. P. A. Belov and Y. Hao, "Subwavelength imaging at optical frequencies using a transmission device formed by a periodic layered metal-dielectric structure operating in the canalization regime," *Phys. Rev. B* **73**, 113110 (2006).
12. X. Li, S. He, and Y. Jin, "Subwavelength focusing with a multilayered Fabry-Perot structure at optical frequencies," *Phys. Rev. B* **75**, 045103 (2007).
13. Y. Jin, "Improving subwavelength resolution of multilayered structures containing negative-permittivity layers by flattening the transmission curves," *Prog. Electromagn. Res.* **105**, 347–364 (2010).
14. A. Salandrino and N. Engheta, "Far-field subdiffraction optical microscopy using metamaterial crystals: theory and simulations," *Phys. Rev. B* **74**, 075103 (2006).
15. K. J. Webb and M. Yang, "Subwavelength imaging with a multilayer silver film structure," *Opt. Lett.* **31**, 2130–2132 (2006).
16. B. Wang, L. Shen, and S. He, "Superlens formed by a one-dimensional dielectric photonic crystal," *J. Opt. Soc. Am. B* **25**, 391–395 (2008).
17. B. Zeng, X. Yang, C. Wang, Q. Feng, and X. Luo, "Super-resolution imaging at different wavelengths by using a one-dimensional metamaterial structure," *J. Opt.* **12**, 035104 (2010).
18. R. Kotynski, T. Stefaniuk, and A. Pastuszczyk, "Sub-wavelength diffraction-free imaging with low-loss metal-dielectric multilayers," arXiv:1002.0658v1.
19. R. Kotynski and T. Stefaniuk, "Multiscale analysis of subwavelength imaging with metal-dielectric multilayers," *Opt. Lett.* **35**, 1133–1135 (2010).
20. Z. Jacob, L. V. Alekseyev, and E. Narimanov, "Optical hyperlens: far-field imaging beyond the diffraction limit," *Opt. Express* **14**, 8247–8256 (2006).
21. Z. Jacob, L. V. Alekseyev, and E. Narimanov, "Semiclassical theory of the hyperlens," *J. Opt. Soc. Am. A* **24**, A52–A59 (2007).
22. A. V. Kildishev and E. E. Narimanov, "Impedance-matched hyperlens," *Opt. Lett.* **32**, 3432–3434 (2007).
23. W. Wang, H. Xing, L. Fang, Y. Liu, J. Ma, L. Lin, C. Wang, and X. Luo, "Far-field imaging device: planar hyperlens with magnification using multi-layer metamaterial," *Opt. Express* **16**, 21142–21148 (2008).
24. M. Yan, W. Yan, and M. Qiu, "Cylindrical superlens by a coordinate transformation," *Phys. Rev. B* **78**, 125113 (2008).
25. H. Lee, Z. Liu, Y. Xiong, C. Sun, and X. Zhang, "Development of optical hyperlens for imaging below the diffraction limit," *Opt. Express* **15**, 15886–15891 (2007).
26. Z. Liu, H. Lee, Y. Xiong, C. Sun, X. Zhang, "Far-field optical hyperlens magnifying sub-diffraction-limited objects," *Science* **315**, 1686 (2007).
27. B. Wood, J. B. Pendry, and D. P. Tsai, "Directed subwavelength imaging using a layered metal-dielectric system," *Phys. Rev. B* **74**, 115116 (2006).
28. B. Stein, J. Y. Laluet, E. Devaux, C. Genet, and T. W. Ebbesen, "Surface plasmon mode steering and negative refraction," *Phys. Rev. Lett.* **105**, 266804 (2010).
29. A. A. Orlov, P. M. Voroshilov, P. A. Belov, and Y. S. Kivshar, "Engineered optical nonlocality in nanostructured metamaterials," *Phys. Rev. B* **84**, 045424 (2011).
30. H. Chen and C. T. Chan, "Electromagnetic wave manipulation by layered systems using the transformation media concept," *Phys. Rev. B* **78**, 054204 (2008).

1. Introduction

In 1873, Abbe [1] determined a physical constraint on the smallest feature resolvable through an ideal optical system, which is known as the diffraction limit. It prevents light from being focused below the order of $\lambda/2$. The reason is that high spatial frequency information carried by evanescent waves only exists in the near field of an object, only the propagating light reaches the far-field image plane. So collecting the evanescent information directly in the near field has long been considered as the most straightforward and effective way to overcome the diffraction limit.

Recently, Pendry [2] proposed that a slab of negative index material (NIM) with $\epsilon = -1$ and $\mu = -1$ can form a perfect copy of an object: all details of the object, even smaller than the wavelength of light are reproduced. This proposed lens can couple incident evanescent waves into resonant surface plasmon, therefore amplify and "restore" evanescent components to exhibit perfect focusing. However, there are no natural NIMs and low-loss isotropic artificial NIMs are difficult to fabricate, especially at the infrared and visible frequencies. So a practical scheme [2] was suggested that one can use a thin layer of silver as a superlens to beat the diffraction limit and obtain subwavelength resolution imaging. This idea was confirmed by

recent experimental results [3] which demonstrated the feasibility of subwavelength imaging using silver slabs in optical frequency range. However, the thickness of this silver film has to be very small as compared to the wavelength and the resolution is restricted by losses in the silver.

Subsequently, recent works [4–6, 10–19] have been devoted to the imaging capabilities of multilayered structures. To reduce the influence of material loss, Ramakrishna and Pendry [5, 6] put forward a realistic structure to improve the subwavelength image in the near-field zone. They cut a metal slab into many thin layers and separated them by alternative metal and dielectric layers. These metal and dielectric layers possess the same thickness, and the real parts of their permittivities have the opposite signs. This structure is equivalent to an array of infinitely conducting wires embedded into the medium with zero permittivity and simply connects object to image point by point [7–9]. But the absence of impedance matching between the structure and surrounding medium (generally in the air) causes strong reflection and restricts slab thickness to be much thinner than the wavelength. Belov and Hao [10, 11] suggested a different physical mechanism called as canalization for subwavelength imaging, which does not involve amplification of evanescent modes. It works as a transmission device which delivers all spatial harmonics, produced by the source including evanescent modes, from front interface of the structure to the back one, provided that the structure has a flat isofrequency contour and the thickness of the slab fulfils Fabry-Perot (FP) resonance condition (an integer number of half-wavelengths). In contrast to the case of Ramakrishna's lens, in the canalization regime the reflection from the slab are absent due to the FP condition which holds for all angles of incidence. However, Li et al. [12] questioned the importance of impedance matching in favor of the FP condition. In fact, for a lossless metal and dielectric, the FP resonance is sufficient to entirely eliminate reflections resulting in perfect imaging without impedance matching. Very recently, Jin [13] further explored multilayered structures to improve subwavelength resolution by flattening the transmission curves. It is found that in the near field imaging, the guided modes inside multilayered structures can amplify some incident evanescent waves for obtaining subwavelength resolution, but usually locally over-amplify them even when material loss exists, which may limit the subwavelength resolution. By choosing appropriate permittivity of dielectric layers, and adding a coating layer to cutoff the corresponding guided modes, they achieved high-subwavelength-resolution imaging. In addition, hyperlens, which resembles Ramakrishna's lens but in a cylindrical profile, is suggested [20–24] and experimentally [25, 26], proved to magnify objects beyond the diffraction limit.

In the present paper, we will investigate how to manipulate the subwavelength imaging through an oblique layered metal-dielectric structure. Lateral image shift will be observed through the planar layered structure, and improving subwavelength resolution can be realized by choosing appropriately the permittivity of dielectric layers according to the chosen negative permittivity of metal layers. Image rotation with arbitrary angles, as well as image magnification, can be produced by the concentric geometry of the alternating layered system.

The forthcoming sections of paper are organized as follows: Section 2 describes the oblique layered structures homogenized using effective medium theory (EMT), and their dispersion relation. Section 3 shows guided modes analysis and transmission properties through the oblique layered system. In section 4, we discuss the lateral image shift with subwavelength resolution through properly designed planar layered structure. Section 5 presents the image rotation effect by the designed concentric geometry. Finally, we summarize the work in Section 6.

2. Oblique layered systems

We begin with an alternating metal-dielectric system with two kinds of isotropic materials whose thicknesses are d_1 and d_2 and permittivities are ϵ_m and ϵ_d , respectively. We further assume that the magnetic field is perpendicular to $x - y$ plane (TM polarization, magnetic field

in the \hat{z} direction) and the time harmonic factor is $\exp(-i\omega t)$. According to EMT, when the thickness of the unit cell ($d_1 + d_2$) is far smaller than the operating wavelength, the effective permittivity of this layered system could be approximated as [27, 30]

$$\varepsilon_x = \frac{(d_1 + d_2)\varepsilon_m\varepsilon_d}{d_1\varepsilon_m + d_2\varepsilon_d}, \varepsilon_y = \frac{d_1\varepsilon_m + d_2\varepsilon_d}{d_1 + d_2} \quad (1)$$

Also, this structure can be regarded as an anisotropic dielectric with a permittivity tensor:

$$\bar{\varepsilon}_{normal} = \begin{bmatrix} \varepsilon_x & 0 \\ 0 & \varepsilon_y \end{bmatrix} \quad (2)$$

Here, we consider two-dimensional systems (the \hat{z} direction is homogenous).

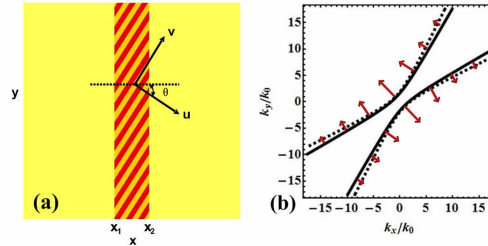


Fig. 1. (color online) (a) The geometry of the planar oblique layered system in the xy plane, the \hat{u} and \hat{v} directions are two principal axes obtained by rotating an angle θ from the \hat{x} and \hat{y} directions, where $\varepsilon_u = \varepsilon_x$ and $\varepsilon_v = \varepsilon_y$. (b) Dispersion relation between k_x and k_y for $\theta = 45^\circ$, $\omega = \omega_0$ (solid line) and $\omega' = 1.05\omega_0$ (dashed line). The slightly variation of constant frequency contour between ω and ω' can determine the direction of the group velocity, which therefore points towards the contour at a higher frequency ω' . The length of arrows is proportional to the magnitude of the group velocity.

Next, we cut the layered system obliquely in the region $x_1 < x < x_2$ shown in Fig. 1(a), then the normal direction of the alternating layers is oriented at a fixed angle, θ , from the \hat{x} direction. Such an oblique layered structure in $x_1 < x < x_2$ can be described as

$$\bar{\varepsilon}_{oblique} = \begin{bmatrix} \varepsilon_{xx} & \varepsilon_{xy} \\ \varepsilon_{yx} & \varepsilon_{yy} \end{bmatrix} = \begin{bmatrix} \cos \theta & \sin \theta \\ -\sin \theta & \cos \theta \end{bmatrix} \begin{bmatrix} \varepsilon_x & 0 \\ 0 & \varepsilon_y \end{bmatrix} \begin{bmatrix} \cos \theta & -\sin \theta \\ \sin \theta & \cos \theta \end{bmatrix} \quad (3)$$

The behavior of such an oblique layered materials can be understood by considering the dispersion relation between the frequency ω and the wave vector \mathbf{k} . We assume that we are dealing with nonmagnetic materials, so that the magnetic permeability $\mu = 1$. Appropriate thickness of the metal and dielectric films in each unit cell could yield positive and negative signs for ε_{xx} , ε_{xy} and ε_{yy} , which represent different forms of dispersion relation

$$k_x^2\varepsilon_{xx} + 2k_xk_y\varepsilon_{xy} + k_y^2\varepsilon_{yy} = \frac{\omega^2}{c^2}(\varepsilon_{xx}\varepsilon_{yy} - \varepsilon_{xy}^2) \quad (4)$$

where c is the velocity of light in vacuum, and k_x and k_y represent the wavevectors in the normal and transversal directions, respectively. Here, typically the parameter ε_{xx} , ε_{xy} and ε_{yy} satisfy the condition $\varepsilon_{xx}\varepsilon_{yy} - \varepsilon_{xy}^2 < 0$, the dispersion function shows a pattern of hyperbola, and k_x is real for a much wider range of values of k_y . Even the high spatial frequency components with large $|k_y|$, which would normally be evanescent, now correspond to real values of k_x , and hence to propagating waves in the media.

The dispersion relation also provides the key to the preferred propagation direction, which is determined by the group velocity $v_g = \nabla_k \omega(k)$ [27, 28]. The preferred propagating direction of the energy flow is normal to the dispersion curve of the constant frequency as shown in Fig. 1(b). It displays two common features. First, the plane wave with large transversal wavevectors, which are evanescent in natural optical materials, could transmit through the metal-dielectric systems. Second, the components with large $|k_y|$ propagate almost in one direction, which is defined by the angle α with respect to the x axis as

$$\alpha = \theta \pm \arctan \sqrt{-\frac{\epsilon_y}{\epsilon_x}} \quad (5)$$

Therefore it is clearly seen that α will be approximated as θ , when $\epsilon_y \ll |\epsilon_x|$.

It is also worthy of noting that Ref. [29] has shown additional eigenwaves may appear which is completely unpredictable by EMT and caused by the plasmonic nature of the layered metal-dielectric structure. But in the presence of high absorption loss in metal at optical frequencies, all the focusing effects may be destroyed. So in this paper (Sec. 4 and Sec. 5) we compare the results between full-wave simulation and homogenized model to validate the focusing effect is still clear, and EMT is a good approximation to the layered structure as before.

3. Mode analysis and transmission through the oblique layered system

We have seen that we can produce a metamaterial with interesting properties by stacking alternating layers of metal and dielectric. Next, we look at a slab of this effective anisotropic material and examine the guided modes and the transmission properties.

We assume that the slab is embedded in a uniform medium of constant permittivity (which may be unity, representing vacuum). In such a medium, the electromagnetic waves satisfy the dispersion relation

$$k_x'^2 + k_y^2 = \frac{\omega^2}{c^2} \epsilon \quad (6)$$

We write k_x' to distinguish the x component of the wave vector in the surrounding medium from that in the slab. Considering the guided wave inside the slab, the fields outside the slab must be evanescent in the longitudinal direction, i.e. $k_x' = i\alpha$, whereas k_x in Eqs. (4) can be real or imaginary which stands for bulk modes and surface modes traveling along the slab, respectively.

Applying the boundary conditions to Maxwell equations, we can obtain the dispersion equations of the slab that define a set of allowed modes:

$$\frac{\alpha}{\epsilon} = \pm \frac{\epsilon_{xx} \Lambda}{\epsilon_{xx} \epsilon_{yy} - \epsilon_{xy}^2} \tan^{\pm} \left(\frac{\Lambda d}{2} \right) \quad (7)$$

where $\Lambda = k_x + \epsilon_{xy} k_y / \epsilon_{xx}$, and (+) and (−) correspond to symmetric (even) and antisymmetric (odd) guided modes, respectively. In the above equations, α , k_x can be expressed in terms of ω and k_y . We thereby obtain a set of transcendental equations, which may be solved graphically or numerically to yield the ω vs. k_y dispersion curves.

It is clear from the dispersion equations that guiding mode solutions are closely related with ϵ_{xx} , ϵ_{xy} , ϵ_{yy} . For simplicity, we choose a metamaterial whose layers are composed of equal thickness of a dielectric, with positive, frequency-independent permittivity, i.e. $\epsilon_d = 4.3$, and a metal with the simple plasmalike permittivity

$$\epsilon_m(\omega) = \epsilon_m(\infty) - \frac{\omega_p^2}{\omega^2} \quad (8)$$

where ω_p is the plasma frequency. For now, we assume that the materials are lossless. Figure 2(a) shows the dispersion curve for the guided modes, where the oblique angle $\theta = 45^\circ$ and the

total thickness of the slab is $\lambda/2$. It is shown that guided modes will be excited at a given ω , i.e. $\omega = \omega_0 = ck_0 = c\frac{2\pi}{\lambda}$, therefore transmission resonances occur which will be shown in Fig. 2(b). Furthermore, we also find that with increasing θ , more and more guided modes appear, and the corresponding wavevectors k_y move toward $\pm k_0$. As a result, this will lead to the excitation of more guided modes for small $|k_y|$ (not shown in this paper). For subwavelength imaging, one wishes to restore the original amplitudes of evanescent waves emitted from the object at the image plane. If perfect restoration is not possible, the amplitudes of some evanescent waves should not be overamplified, otherwise, strong side-lobes may appear and destroy the imaging. Thus, the existence of guided modes, in particular for small $|k_y|$, is harmful for subwavelength imaging.

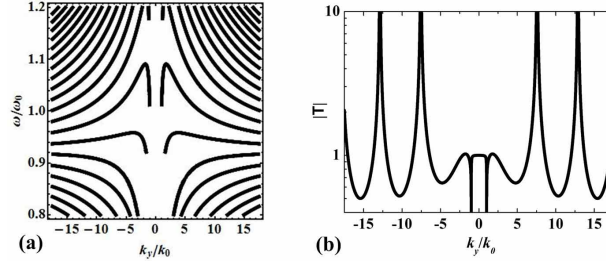


Fig. 2. (a) Dispersion relation with guiding bands. (b) Transmission curves of a lossless anisotropic medium at a given $\omega = \omega_0$. The permittivity of the metal is given by (8) with $\epsilon_m(\infty) = 1.0$. The layers are of equal width $d_1 = d_2 = \lambda/40$.

To see the functionality of subwavelength-imaging clearly, we usually calculate the transfer function, which is defined as the ratio of the field at the image plane to that at the object plane. For our case, the transfer function has the form

$$T = \frac{2 \exp \left[-idk_y \frac{\epsilon_{xy}}{\epsilon_{xx}} \right]}{2 \cos(\Lambda d) + i \sin(\Lambda d) \left[\frac{(\epsilon_{xy}^2 - \epsilon_{xx}\epsilon_{yy})k'_x}{\epsilon\epsilon_{xx}\Lambda} + \frac{\epsilon\epsilon_{xx}\Lambda}{(\epsilon_{xy}^2 - \epsilon_{xx}\epsilon_{yy})k'_x} \right]} \quad (9)$$

In Fig. 2(b), we plot the transfer function from the object plane to the image plane across a lossless slab for the oblique angle $\theta = 45^\circ$. Due to the excitation of the guided modes, transmission resonances appear. It is worthy noting that transmission curves show a wide flat upheaval for small $|k_y|$, which is very beneficial for subwavelength imaging. Also, it is noticed that due to mismatched impedance, there is some reflection for $|k_y| < k_0$ on the input interface, but not very large. This may reduce the intensity of the image, but influence little the resolution. In addition, due to the translation invariance of the structure along the y direction, the transmission for negative k_y is the same as that for positive k_y . However, the symmetry will be broken for lossy cases as seen next.

In the above and following analysis, the parameter ϵ_d we used is larger than $-Re(\epsilon_m)$, otherwise, the incident propagation waves will be reflected strongly, which is not good for imaging. Also we can obtain flat upheavals of transmission curves which can improve the image quality greatly.

4. Shift of subwavelength image

We have seen that this oblique layered system allows to change preferred propagation direction, which is mainly determined by the oblique angle, and also it can provide enhanced transmission

of high-spatial-frequency components at certain frequencies. This gives us hope that we may achieve lateral shift of imaging with high resolution by using this system.

As a test, we consider the image of a point source. In this paper, when imaging is carried out, a point source as an object is put on the left (or inner) surface of the structure, and the image plane is defined on the right (or outer) surface. The parameters are used as before, except for the permittivity of the metal. In practice, material loss always exists in a natural negative-permittivity material. To investigate the influence of material loss on the above oblique layered system, we take the metal permittivity $\epsilon_m = -3.5 + 0.23i$ at a particular optical frequency $\omega = \omega_0$. Full wave EM simulation based on the two-dimensional finite element method is performed to verify the subwavelength resolution imaging.

Let's firstly see the image-shifting due to the variation of oblique angles θ . Figs. 3(a)–3(e) show the image of a point source through the effective anisotropic medium, when θ changes from 0° to $15^\circ, 30^\circ, 45^\circ$, and 60° . Here, $\epsilon_d = 4.3$ is unchanged. The source is put at $y = 0$ at the left of the structure. the imaging point does not locate at $y = 0$, but makes a displacement, $\Delta y = (x_1 - x_2) \tan \theta$, due to the designed oblique structure. As we expect, as θ increasing from 0° to $15^\circ, 30^\circ, 45^\circ, 60^\circ$, the displacements Δy can be observed as $0, -0.13\lambda, -0.29\lambda, -0.51\lambda, -0.90\lambda$, respectively. To see clearly the image intensity and resolution, we plot in Fig. 4(a) the distribution of magnetic energy density at the image plane. For $\theta = 0^\circ$, the full width at half maximum (FWHM) of image is about 0.08λ , with high intensity. While increasing θ to 60° , the FWHM of image increases to 0.2λ , and the image becomes dimmer. Moreover, strong side-lobes appear and destroy the imaging. This phenomenon of variation of image resolution and intensity as θ increases can be well understood according to transmission curves shown as Fig. 5. With loss introduced, the transmission $|T|$ drops quickly for large $|k_y|$. However, fortunately, such dropping of $|T|$ for large $|k_y|$ does not influence significantly high resolution imaging. The amplitudes of evanescent wave with small $|k_y|$ are usually larger than those with large $|k_y|$. That is, evanescent waves with small $|k_y|$ are more important to generate a subwavelength image and evanescent waves with large $|k_y|$ are of little importance. Therefore, for $\theta = 0^\circ, 15^\circ, 30^\circ$, it can still generate a good subwavelength-image through this structure. However, for larger oblique angle, i.e. $\theta = 45^\circ, 60^\circ$, material loss enhances further the quick dropping of the transmission $|t|$, which influences significantly high-resolution imaging.

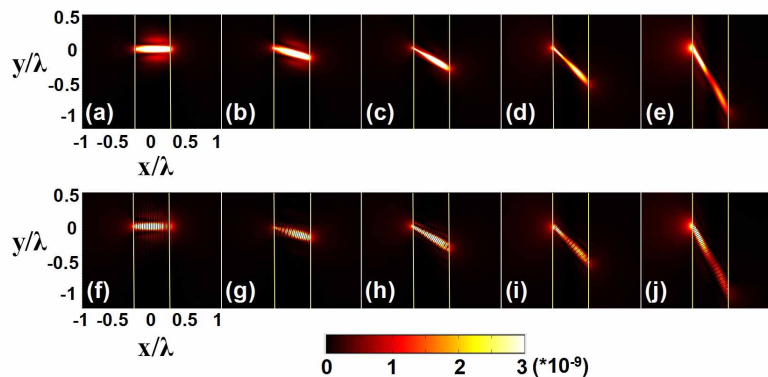


Fig. 3. (color online) The distribution of magnetic energy density (a)-(e) for an effective anisotropic medium, and (f)-(j) for an oblique planar layered system in the $x - y$ plane, with $\theta = 0^\circ, 15^\circ, 30^\circ, 45^\circ$, and 60° , respectively. Here, the permittivity of metal $\epsilon_m = -3.5 + 0.23i$, and the permittivity of dielectric $\epsilon_d = 4.3$. The yellow solid lines indicate the boundaries of the systems.

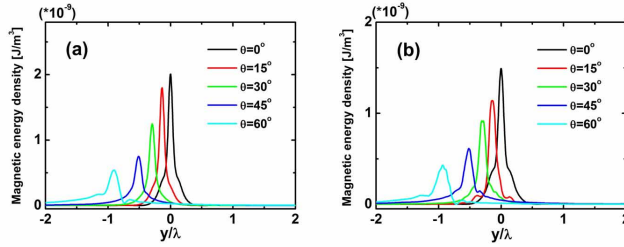


Fig. 4. (color online) Comparison of magnetic energy density of the image plane along the y direction between (a) the effective anisotropic medium and (b) the planar layered systems for different oblique angle.

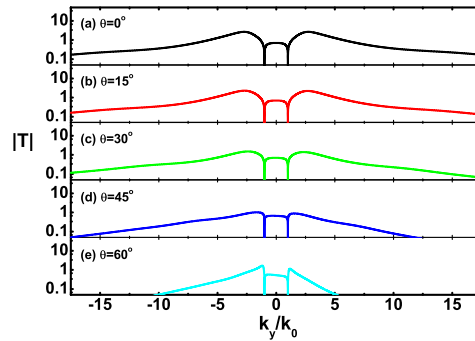


Fig. 5. (color online) Transmission curves of a lossy anisotropic medium for different θ (a) 0° , (b) 15° , (c) 30° , (d) 45° , (e) 60° .

Treating the layered system as an effective medium is a helpful simplification and the EMT analysis can give us enough guidance. To confirm the above result, we represent in Figs. 3(f)–3(j) the image of the point source through the oblique layered system for different θ . The distributions of magnetic energy density look quite similar to those shown Figs. 3(a)–3(e) for the corresponding effective anisotropic media. To see clearly, Fig. 4(b) also shows the corresponding distribution at the image plane for the oblique layered system. The comparison between Fig. 4(a) and Fig. 4(b) validates the appropriateness of the EMT, as the layers are made thin enough.

Next, we investigate how the image-shifting is influenced by tuning the dielectric permittivity ϵ_d of the corresponding multilayered structure. Figs. 6(a)–6(e) show the distribution of magnetic energy density for the effective anisotropic medium, when ϵ_d increases from 3.5 to 4.0, 4.3, 4.8, to 6.0. Here, θ is fixed, i.e. $\theta = 30^\circ$. For different ϵ_d , it always indicates the same shift of imaging. However, with ϵ_d increasing, the imaging quality will be influenced greatly, as clearly seen from Fig. 7(a). For $\epsilon_d = -Re(\epsilon_m) = 3.5$, the lossy structure can not work well for subwavelength imaging, whereas a high image resolution is obtained for the case of $\epsilon_d = 4.0, 4.3, 4.8$, and the FWHM is about $\lambda/10$ for $\epsilon_d = 4.3$. However, further increasing ϵ_d will reduce the image quality, even the location of shift-imaging is changed slightly. The explanation can also be obtained from the transmission curves shown in Fig. 8. From these transmission curves, we can see material loss damps the sharp transmission peaks, but they remain sharp for $\epsilon_d = 3.5$, and over-amplification of some evanescent waves can not be eliminated completely, which may deteriorate the image quality. Thus it can not work well for subwave-

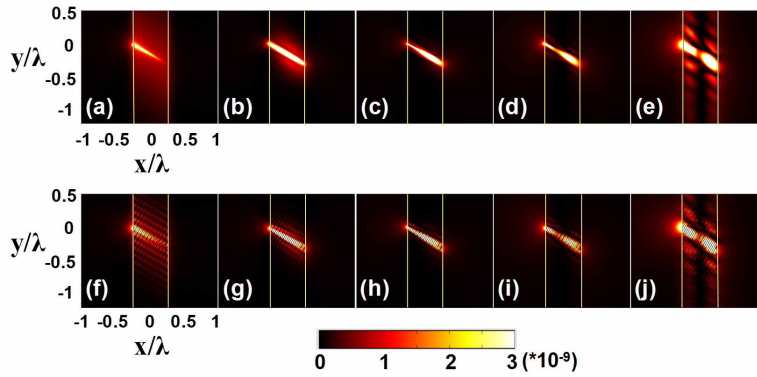


Fig. 6. (color online) The distribution of magnetic energy density (a)–(e) for an effective anisotropic medium, and (f)–(j) for an oblique planar layered system in the $x - y$ plane, with different permittivity of dielectric $\epsilon_d = 3.5, 4.0, 4.3, 4.8,$ and $6.0,$ respectively. Here, the permittivity of metal $\epsilon_m = -3.5 + 0.23i,$ and the oblique angle $\theta = 30^\circ.$ The yellow solid lines indicate the boundaries of the systems.

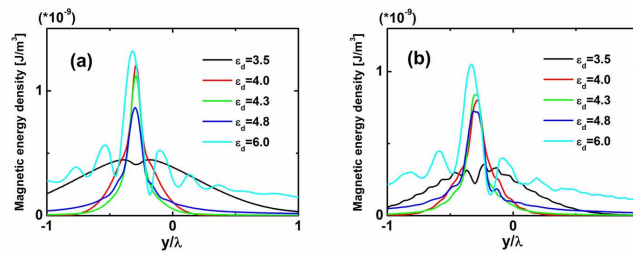


Fig. 7. (color online) Comparison of magnetic energy density of the image plane along the y direction between (a) the effective anisotropic medium and (b) the planar layered systems for different permittivity of dielectric.

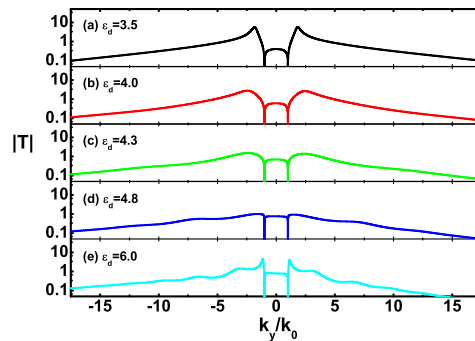


Fig. 8. (color online) Transmission curves of a lossy anisotropic medium for different permittivity of dielectric ϵ_d (a) 3.5, (b) 4.0, (c) 4.3, (d) 4.8, and (e) 6.0.

length imaging, due to the existence of sharp transmission. With ϵ_d increasing and deviating away from 3.5, they display a flat pattern near k_0 for $\epsilon_d = 4.0, 4.3$ and 4.8 , which is beneficial for subwavelength imaging. As ϵ_d increases further, a new sharp peak is generated near k_0 , and material loss decreases the image resolution. The oblique layered structure is used to confirm the above result. In Figs. 6(f)–6(j) we plot the magnetic energy for the oblique layered structure with $\theta = 30^\circ$ in case of $\epsilon_d = 3.5, 4.0, 4.3, 4.8$ and 6.0 . The magnetic energy distributions look quite similar to those shown in Figs. 6(a)–6(e). A detailed comparison between Fig. 7(a) and Fig. 7(b) for the energy distribution at the image plane also shows the accuracy of EMT.

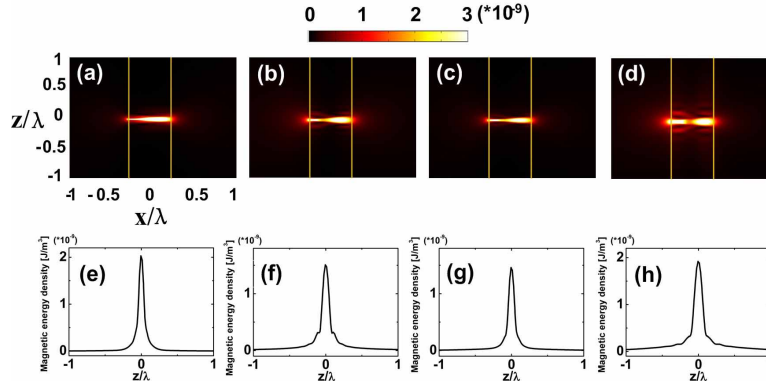


Fig. 9. (color online) The distribution of magnetic energy density for an effective anisotropic medium in the $x-z$ plane. (a) $\theta = 30^\circ, \epsilon_d = 4.3$, (b) $\theta = 30^\circ, \epsilon_d = 4.8$, (c) $\theta = 45^\circ, \epsilon_d = 4.3$, (d) $\theta = 45^\circ, \epsilon_d = 4.8$. (e)–(h) the corresponding detailed distribution at the image plane along the z direction. The yellow solid lines indicate the boundaries of the systems.

So far, the subwavelength imaging is only considered in the $x-y$ plane, which corresponds to one-dimensional imaging. Actually, we can realize two-dimensional subwavelength imaging in the proposed oblique multilayered structure. To see the two-dimensional imaging effect, we show in Figs. 9(a)–9(b) the image of a point source in the $x-z$ plane through the effective anisotropic medium for $\epsilon_d = 4.3, 4.8$, respectively. We take other parameters: the oblique angle $\theta = 30^\circ$, $\epsilon_m = -3.5 + 0.23i$ in two cases. Obviously from the simulation the good image quality can also be achieved in $x-z$ plane. The FWHM of image is about $\lambda/10$ shown respectively in Figs. 9(e)–9(f). Subsequently, tuning the oblique angle $\theta = 45^\circ$, we still achieve the image with subwavelength resolution in Figs. 9(c)–9(d). The corresponding distributions of magnetic energy density at the image plane are shown in Figs. 9(g)–9(h). Thus we can confirm our proposed structure can work well for two-dimensional subwavelength imaging.

5. Rotation effect of subwavelength image

By using the above concept of the image shifter with oblique planar layers, we then can realize an image rotator using a concentric layered systems. In Fig. 10(a), we illustrate the geometry of the layered system to produce the rotation effect of subwavelength imaging. The detailed shape of each layer is as follow: by using certain curves, we divide the concentric shell ($a < r < b$, a and b are radius of inner and outer radii of the system, respectively) into N layers for the alternating material of dielectric or metals. For these curves, we have the formula in the cylindrical coordinates (r, ϕ, z) [the \hat{z} direction is homogenous] [30]

$$\phi = \beta - \cot(\theta) \ln\left(\frac{a}{r}\right) \quad (10)$$

with the starting point in the inner circle, $r = a$ and $\phi = \beta$. Here, θ is the oblique angle, and $\beta = 0, 2\pi/N, 4\pi/N, \dots, 2(N-1)\pi/N$. Starting with these N points, we can produce N curves that will divide the concentric shell ($a < r < b$) into N fan shaped parts [see Fig. 10(a)]. Then if the number of the alternating layers is large enough, the concentric layered structure with alternating layers of dielectric and metal can be used to mimic the anisotropic properties in the \hat{r} and $\hat{\phi}$ directions very precisely. We use these alternating layers of dielectric and metallic (ϵ_d and ϵ_m) materials the same way as before. According to the EMT, we can obtain the permittivity tensor for an image rotator within the shell region ($a < r < b$) in the Cartesian coordinates [30]:

$$\bar{\epsilon}_{rotator} = \begin{bmatrix} \cos \theta & -\sin \theta \\ \sin \theta & \cos \theta \end{bmatrix} \begin{bmatrix} \cos \phi & -\sin \phi \\ \sin \phi & \cos \phi \end{bmatrix} \begin{bmatrix} \epsilon_x & 0 \\ 0 & \epsilon_y \end{bmatrix} \times \begin{bmatrix} \cos \phi & \sin \phi \\ -\sin \phi & \cos \phi \end{bmatrix} \times \begin{bmatrix} \cos \theta & \sin \theta \\ -\sin \theta & \cos \theta \end{bmatrix}. \quad (11)$$

Through this image rotator as shown in Fig. 10(b), we then see the image rotation, as well as magnification with subwavelength resolution. It has an inner radius a and an outer radius of b . With the material parameter obtained above, 2D subwavelength objects at the inner surface will be imaged at the outer surface of the structure. For example, point sources at S_1, S_2 , and S_3 of the source plane will be restored well at I_1, I_2 , and I_3 of the image plane, respectively. Such a structure acts as an optical image component that makes perfect image between source and image plane with the rotation of $\tan(\theta) \ln(b/a)$ [30] in the limit of subwavelength resolution. Further, the interesting feature of the image rotator is that the image size is not equal to that of the object with a magnification determined by

$$\frac{I_i I_j}{S_i S_j} = \frac{b}{a} \quad (i, j = 1, 2, 3, i \neq j) \quad (12)$$

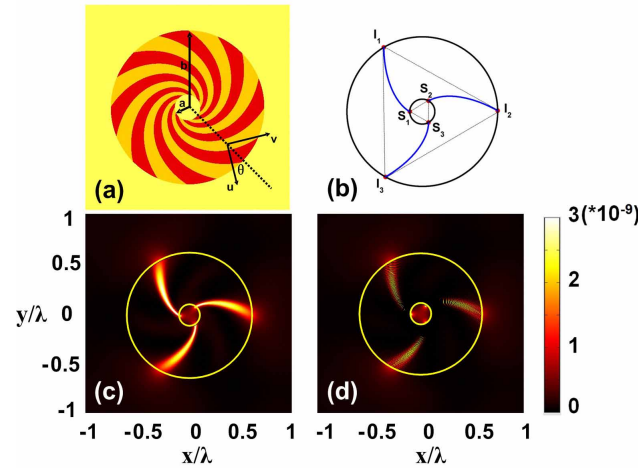


Fig. 10. (color online) (a) The geometry of the concentric oblique layered system in the xy plane, the \hat{u} and \hat{v} directions are two principal axes obtained by rotating an angle θ from the \hat{r} and $\hat{\phi}$ directions, where $\epsilon_u = \epsilon_x$ and $\epsilon_v = \epsilon_y$. (b) Schematic of the image rotator configuration. (c)(d) The distribution of magnetic energy density for an effective anisotropic medium and the concentric layered system, respectively. Here, the permittivity of metal $\epsilon_m = -3.5 + 0.23i$, the permittivity of dielectric $\epsilon_d = 4.0$, and the oblique angle $\theta = 30^\circ$. The yellow solid lines outline the interior and exterior boundaries of systems.

To verify the performance, we also carry out full wave EM simulation of the proposed the image rotator. Figure 10(c) shows the rotated image of subwavelength resolution can be obtained on the effective anisotropic medium. The image rotator has an inner radius of $a = 0.1\lambda$ and an outer radius of $b = 0.6\lambda$, Three point sources S_1, S_2 , and S_3 are located at the inner boundary $(-a, 0), (a/2, -\sqrt{3}a/2), (a/2, \sqrt{3}a/2)$, respectively. Here, $\theta = 30^\circ$, $\epsilon_d = 4.0$ and $\epsilon_m = -3.5 + 0.23i$. It is clearly demonstrated that well resolved images of the three point sources appear at the outer surface with positions of $(-b/2, \sqrt{3}b/2), (b, 0), (-b/2, -\sqrt{3}b/2)$, which confirms the ability of the structure of imaging subwavelength objects. The structure achieves an image with the magnification of $b/a = 6$, the resolution of image is about $\lambda/10$, and the rotation angle of image is nearly 60° as clearly shown in Fig. 11. It is worth noting that small material loss does not influence significantly high-resolution imaging. The key is to transmit evanescent waves in a wide range through the lens structure in appropriate proportion. We also give the imaging through the concentric layered metal-dielectric structure with $N = 72$ in Fig. 10(d). Appropriateness of the EMT is confirmed by similar distributions of magnetic energy density.

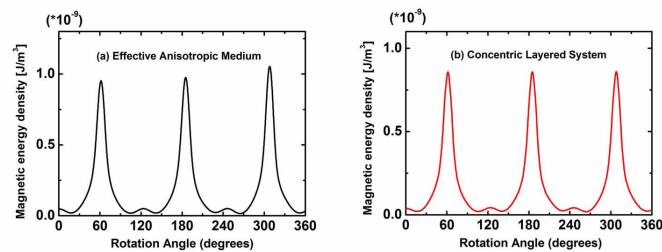


Fig. 11. (color online) Comparison of magnetic energy density of the image plane along the ϕ direction between (a) the effective anisotropic medium and (b) the concentric layered systems for $a = 0.1\lambda$, $b = 0.6\lambda$, and $\theta = 30^\circ$.

Such magnified image can be further processed by conventional optics and the rotation effect of subwavelength image greatly increases the flexibility of beam control. This design only requires simple isotropic materials without spatial gradient. Since the suggested method is general, it can be applied for other negative permittivities.

6. Conclusion

In this paper, we extend the concept of subwavelength imaging and manipulate subwavelength images flexibly through an oblique layered system. We demonstrate that image shifting could be achieved through an oblique planar layer system, and image rotation with arbitrary angle as well as magnified image could be obtained through an concentric layered system. The theoretical analysis and design procedure of these image processing components have been given, and their performances have been confirmed by full wave EM simulation. The proposed structures can be deployed as a basic element to manipulate light for further optical processing of the image by conventional optics.

Acknowledgments

This work was supported in part by the National Science Foundation of China under Grant Nos. 10647114, 60990320, 60990324, 60871016, and 60901011, in part by the Natural Science Foundation of Jiangsu Province under Grant No. BK2008031, and in part by the 111 Project under Grant No. 111-2-05. J. Wang is grateful for support from China Scholarship Council and Southeast University.